A Cyclone-Centered Perspective on the Drivers of Asymmetric Patterns in the Atmosphere and Sea Ice during Arctic Cyclones[⌀]

ROBIN CLANCY,[a] CECILIA M. BITZ,[a] EDWARD BLANCHARD-WRIGGLESWORTH,[a] MARIE C. MCGRAW,[a] AND
STEVEN M. CAVALLO[b]

[a] *University of Washington, Seattle, Washington*
[b] *University of Oklahoma, Norman, Oklahoma*

ABSTRACT: Arctic cyclones are an extremely common, year-round phenomenon, with substantial influence on sea ice. However, few studies address the heterogeneity in the spatial patterns in the atmosphere and sea ice during Arctic cyclones. We investigate these spatial patterns by compositing on cyclones from 1985 to 2016 using a novel, cyclone-centered approach that reveals conditions as functions of bearing and distance from cyclone centers. An axisymmetric, cold-core model for the structure of Arctic cyclones has previously been proposed; however, we show that the structure of Arctic cyclones is comparable to those in the midlatitudes, with cyclonic surface winds, a warm, moist sector to the east of cyclones and a cold, dry sector to the west. There is no consensus on the impact of Arctic cyclones on sea ice, as some studies have shown that Arctic cyclones lead to sea ice growth and others to sea ice loss. Instead, we find that sea ice decreases to the east of Arctic cyclones and increases to the west, with the greatest changes occurring in the marginal ice zone. Using a sea ice model forced with prescribed atmospheric reanalysis, we reveal the relative importance of the dynamic and thermodynamic forcing of Arctic cyclones on sea ice. The dynamic and thermodynamic responses of sea ice concentration to cyclones are comparable in magnitude; however, dynamic processes dominate the response of sea ice thickness and are the primary driver of the east–west difference in the sea ice response to cyclones.

KEYWORDS: Arctic; Sea ice; Extratropical cyclones

1. Introduction

Arctic cyclones (ACs) can have a major influence on the Arctic atmosphere and sea ice in their vicinity. Individual ACs act on time scales of days to weeks and can cause regional sea ice variability on these time scales (Schreiber and Serreze 2020; Wang et al. 2020), with important implications for short-term sea ice forecasting (Lukovich et al. 2021). ACs occur frequently, with approximately three ACs typically present north of 65°N at any given time in each season (as we will show). As a result, their local impacts integrate to control the climatology and variability of the large-scale Arctic atmosphere (Lee and Kim 2019; Fearon et al. 2020) and influence the interannual variability in pan-Arctic sea ice extent (Screen et al. 2011). Characterization of the structure and impacts of ACs is, therefore, necessary for a full understanding of Arctic variability on a range of scales in space and time.

Arctic cyclones are often distinguished from midlatitude cyclones by their high latitude; however, separation of the two storm types based on differences in their structure, behavior and formation is not always clear. One complication is that approximately half the cyclones in the Arctic originate as midlatitude cyclones (Vessey et al. 2020). A conceptual model of the structure of summer ACs was proposed by Aizawa and Tanaka (2016), including a warm core in the stratosphere and cold core in the troposphere, with axisymmetric winds, temperatures, and vertical motion. They suggest that a diameter of 5000 km is typical for ACs, as are cyclonic surface winds. They also underscore the importance of coupling with upper-level tropospheric polar vortices, as identified in other studies (e.g., Hoskins et al. 1985; Simmonds and Rudeva 2014), the structure of which is described in Cavallo and Hakim (2010). Arctic cyclones can have a lifetime of up to 3 weeks, much longer than that of midlatitude cyclones (Yamagami et al. 2017).

Historically, the study of the effects of ACs on sea ice has been dominated by case studies of individual cyclones. For example, the Great Arctic Cyclone of August 2012, which features prominently in the literature as an example of AC-driven rapid sea ice loss (Simmonds and Rudeva 2012; Zhang et al. 2013). Such case studies are valuable in identifying the processes acting on the atmosphere and sea ice during an event, such as the development of ACs from tropopause polar vortices (Simmonds and Rudeva 2012), the importance of preconditioning in determining the sea ice response (Parkinson and Comiso 2013), the role of warm air advection and subsequent surface melt (Stern et al. 2020) and the role of surface winds in driving sea ice melt through the driving of ocean mixing and upwelling of warm water (Zhang et al. 2013; Peng et al. 2021). However, extrapolation of these case studies to draw conclusions on the typical effects of ACs on sea ice is problematic, as sample sizes are small and cyclones resulting in large sea ice loss events are likely oversampled.

An alternative method of determining the typical effects of ACs on sea ice is to statistically analyze a very large number of cyclones. In doing so, natural variability in the Arctic

atmosphere and sea ice may be averaged out, albeit at the expense of information about the variability among ACs. In principle, this approach provides an objective means of establishing the effects of cyclones on sea ice, however, different statistical approaches have come to a variety of often contradictory conclusions.

A subset of statistical studies has explored the relationship between the number or intensity of ACs in a year and sea ice extent. September sea ice extent has been found to increase with higher cyclone frequency in early summer (Screen et al. 2011) and decrease with more intense summer cyclones (Simmonds and Keay 2009), particularly in certain regions (Semenov et al. 2019). Rae et al. (2017) reveal that this approach may result in very different results depending on the methods by which ACs are tracked and the time period sampled, with both positive and negative relationships between cyclone number or intensity and September sea ice extent. The relationships revealed between ACs and sea ice loss are also not necessarily causal. Confounding variables such as the sign of the northern annular mode (NAM) may result in spurious correlations and, in a reversal of causality, sea ice anomalies may lead to conditions favoring cyclogenesis (Koyama et al. 2017; Screen et al. 2018).

Another subset of statistical studies have composited atmosphere and sea ice variables at each grid cell on dates when that grid cell is under the influence of an AC. Schreiber and Serreze (2020) show that in each season there are regions of the Arctic where the influence of ACs causes sea ice extent to either grow quicker or decline slower than usual, resulting in an increase in sea ice concentration (SIC). Similarly, Finocchio et al. (2020) find reduced sea ice melt within 500 km of an AC during early summer in the marginal ice zone. These studies are useful in determining the mechanisms driving the response of sea ice to ACs, and regional variations in this response. However, by condensing the effects of an AC to a single averaged value at each location these results mask spatial heterogeneity in the sea ice response.

From both case studies and statistical studies (Overland and Pease 1982) it has long been known that the response of sea ice to ACs varies based on both the distance and direction from a cyclone. Rapid sea ice loss has been shown to occur to the east of ACs, as part of a dipole with anticyclones that drives the poleward transport of heat and water vapor into the Arctic (Wang et al. 2020). A full spatial footprint of the effect of ACs on SIC was developed through compositing the sea ice response to individual ACs by Kriegsmann and Brümmer (2014), who found that cyclones tend to reduce SIC near their center in all seasons. However, several factors limit their conclusions. Only 3 years of ACs were analyzed and their central Arctic domain choice omits the response of the marginal ice zone, in which more recent studies suggest the greatest sea ice response occurs (Semenov et al. 2019; Schreiber and Serreze 2020; Finocchio et al. 2020). Furthermore, individual footprints contributing to the composite are oriented such that the top of the footprint is in a somewhat arbitrary direction from the AC, as opposed to consistently being north of the AC.

While the effect of ACs on sea ice remains an unresolved question, so too does the relative importance of dynamic and

thermodynamic processes in driving these effects. Dynamic processes include the transport and deformation of sea ice, primarily in response to surface winds (Thorndike and Colony 1982). Thermodynamic processes include the melting and freezing of sea ice in response to energy fluxes from either the atmosphere or the ocean. In a study of extreme ACs in the summers of 2012 and 2016, Lukovich et al. (2021) suggest that depending on the location and timing of an AC either thermodynamic processes dominate the sea ice response or that dynamics may be of comparable importance. However, small sample sizes are again a consideration and as climatology is not removed in this study a portion of the thermodynamic changes identified in this study may be typical summer sea ice melt and not the result of the presence of an AC.

In this study we aim to establish the spatial pattern of the average effects of an AC on Arctic sea ice concentrations recorded by satellite and explain the role of the atmosphere in driving these. Cyclone data are derived from different tracking algorithms applied to two reanalyses. We develop a consistent cyclone-centered reference frame based on the distance and bearing from an AC along lines of constant azimuth, revealing differences in the response of sea ice to the east and west of an AC. The spatial patterns of the average atmospheric properties of ACs and the associated surface radiative and dynamic forcing are established by compositing atmospheric reanalysis on AC positions. Finally, we use a sea ice model forced with atmospheric reanalysis to quantify the importance of dynamic and thermodynamic processes in determining the pattern of the effects of ACs on sea ice. Through these analyses we are able to shed light on heterogeneity in the spatial pattern of sea ice response to ACs and attribute this pattern to primarily dynamic processes, while also demonstrating the important role of thermodynamic processes at the ice top and base, all of which can be connected back to spatial patterns in atmospheric variables during ACs.

2. Data and methods

In this study we analyze the atmospheric structure, surface energy fluxes and sea ice patterns by compositing relevant quantities during Arctic cyclones. We use AC location and intensity from two cyclone-tracking algorithms as summarized in Table 1. The other sources of data that we use, ERA5 atmospheric dataset (Hersbach et al. 2020), SIC observations and a sea ice model, are also summarized in Table 1. The ERA5 has been shown to perform well in many metrics in the Arctic compared to other reanalyses (Graham et al. 2019; Mayer et al. 2019).

The first cyclone dataset is derived from ERA-Interim by Sprenger et al. (2017). We distinguish ACs from other extratropical cyclones by selecting only cyclones above 65°N. We focus our analysis on ACs in the upper quartile of intensity by season defined based on their amplitude, that is the maximum SLP within a closed contour around an AC minus the minimum SLP within this contour at the same instant, as the dataset includes many very weak cyclones. The majority of our results are based on AC tracks from Sprenger et al. (2017) for the full period 1985–2016; however, there are two exceptions in which

TABLE 1. Datasets used and descriptions.

Data type	Data source/notes	Dates	Resolution
Arctic cyclone tracks	Serreze (2009) with NCEP–NCAR reanalysis	1985–2016	6-h temporal resolution, 250-km spatial resolution
	Sprenger et al. (2017) with ERA-Interim	1985–2016	6-h temporal resolution, 1° spatial resolution
Atmospheric reanalysis—ERA5	Only data north of 65°N are used. Surface energy fluxes defined positive downward	1985–2016	6-h temporal resolution, 0.25° spatial resolution
SIC	NASA Goddard bootstrap daily sea ice concentrations (Comiso 2017). Only data north of 65°N are used	1985–2016	Daily temporal resolution after summer 1987; every other day before. 25-km spatial resolution
CICE5 sea ice dynamical model	CICE5 forced with JRA-55, coupled to a slab ocean	1985–2016	Daily temporal resolution. Nominally 1° with the model's North Pole displaced into Greenland

we deviate from this. First, we test the stationarity of our results by examining the spatial patterns associated with ACs in two separate, nonoverlapping periods of 16 years each (1985–2000 and 2001–16). Second, we investigate the influence of differences in the choice of cyclone-tracking algorithm by using AC tracks derived from NCEP–NCAR reanalysis of SLP data by Serreze (2009), with additional screening following Serreze and Barrett (2008). These tracks also span 1985–2016. To further distinguish the two cyclone datasets, the local Laplacian of ACs is used instead of the amplitude to select the upper quartile of most intense cyclones from the Serreze (2009) dataset.

The number of AC observations used for each season in each year is shown in Fig. 1, as is the minimum amplitude threshold for each season. We define our seasons as winter [December–February (DJF)], spring [March–May (MAM)], summer [June–August (JJA)], and fall [September–November (SON)]. Before application of our minimum amplitude threshold approximately three ACs are present above 65°N at any given time in each season; however, after our threshold is applied this value falls to approximately 0.7. In each season, the trend in the number of AC observations is not significantly different from 0 at a 90% significance level. The ACs in fall and winter are of greater amplitude than those in spring and summer. The probability of

occurrence of an AC within 500 km of each gridbox center in each season is shown in Fig. 2. Local maxima in the probability of occurrence of an AC are found in the Norwegian, Greenland, and Barents Seas in all seasons, and in the central Arctic and Canadian Archipelago in summer and fall. Equivalent plots for AC counts and locations for Serreze (2009) tracks are included in Figs. S1 and S2.

To distinguish the thermodynamic and dynamic effects of ACs on sea ice, we use a preexisting integration of the CICE5 sea ice model (Hunke et al. 2015), forced with Japan 55-year Reanalysis (JRA-55; Japan Meteorological Agency 2013; Kobayashi et al. 2015), coupled to a slab ocean. Different reanalyses, such as ERA5 and JRA-55, show different biases in the Arctic (Graham et al. 2019; Mayer et al. 2019); however, the uncertainty arising from the atmospheric forcing is likely much smaller than that arising from uncertainty in the ice and ocean physics parameterizations in CICE5. The atmospheric forcing for year 1975 was repeated 30 times while the model spun up, followed by forcing for years 1975–2016. Output from 1985 to 2016 is used for our analysis. Including results from this simulation allows us to investigate the sea ice thickness (SIT) simulated by CICE5, while observations of SIT are too short for our purpose. We note that SIT is the gridcell average over the ice covered and open water portions of the grid cell, therefore SIT is
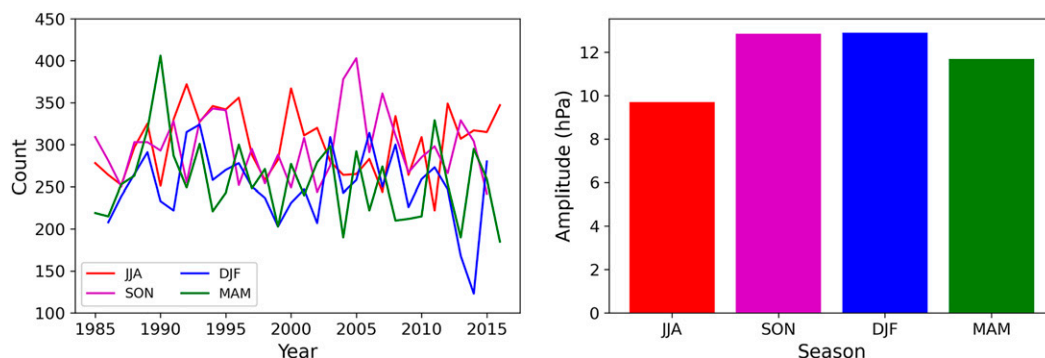

FIG. 1. (left) Arctic cyclone count in each season in each year after selecting the upper quartile of ACs by intensity. (right) Minimum cyclone intensity threshold for each season, calculated as the upper quartile of Arctic cyclone amplitude. These data are taken from Sprenger et al. (2017) cyclone tracks above 65°N.
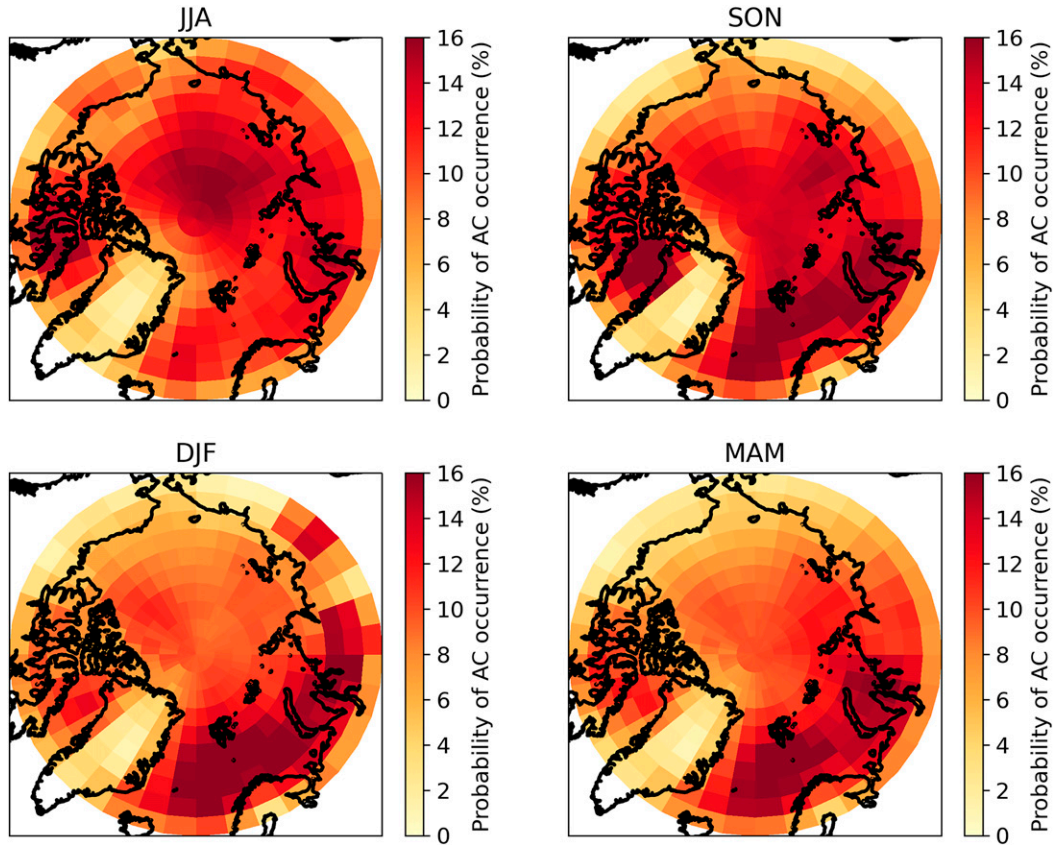
FIG. 2. Probability of Arctic cyclone occurrence within 500 km of the center of each grid point in each season after selecting the upper quartile of cyclones by intensity.

proportional to the volume of sea ice in the grid cell. We also investigate the components of the mass balance that contribute to SIT changes (e.g., top melt and basal melt) using results from CICE5.

Anomalies are computed by removing the 1985–2016 mean annual cycle from each ERA5 and CICE5 variable and SIC observations. The mean annual cycle is computed for each location and at the time interval of the dataset (i.e., 6-hourly for ERA5 or daily for SIC). Linear interpolation is used to fill missing days in observed SIC data prior to summer 1987 when calculating the climatology; however, SIC anomalies are not calculated for interpolated days. When our analysis is split into earlier (1985–2000) and later (2001–16) periods the mean annual cycle is calculated using only values from those years.

To composite the spatial patterns of variables associated with ACs, we developed a method to regrid each dataset to cyclone-centered coordinates. In other words, a cyclone-centered perspective is applied, permitting an analysis of a variable as a function of its position relative to an AC. To do so, we use lines of constant azimuth, known as rhumb lines or loxodromes, which appear as straight lines on a Mercator projection. For each AC, the distance and bearing along rhumb lines to each point in the observational, reanalysis, or model grid is calculated. The result is a grid in polar coordinates with values of a variable associated with them. The

equations for calculating the distance and bearing between two points along a rhumb line are as follows:

$$\Delta\psi = \ln\left[\frac{\tan\left(\frac{\pi}{4} + \frac{\varphi_2}{2}\right)}{\tan\left(\frac{\pi}{4} + \frac{\varphi_1}{2}\right)}\right],$$

$$q = \frac{\Delta\varphi}{\Delta\psi},$$

$$r = \sqrt{\Delta\varphi^2 + q^2 \Delta\lambda^2} \cdot R,$$

$$\theta = \text{atan2}(\Delta\lambda, \Delta\psi),$$

where r is the distance, θ is the bearing, φ is latitude, λ is longitude, and R is Earth's radius.

The results for each AC are then spatially averaged by taking the mean of each variable within bins spaced every 50 km from the AC center to a radius of 1500 km and every 10° from 0° to 360°, following the equation

$$x_{i,j,k} = \overline{x_k} \begin{cases} d_i \leq r < d_{i+1} + 50\,\text{km} \\ \text{and} \\ a_j \leq \theta < a_{j+1} + 10° \end{cases},$$

where x is the variable being composited, d_i are the distances of the bin edges, a_j are the bearings of the bin edges, and k is a unique index for each AC observation. A demonstration of this regridding process is provided in Fig. 3. Spatial compositing is then performed by taking the mean across AC observations:

$$x_{i,j} = \overline{x_{i,j,k}}.$$

For analysis of surface energy flux and sea ice variables, only anomalies over *sea ice regions* are chosen to contribute toward the composite. To do this we give these fields a weighting of 1 in grid cells where the SIC climatology is above 0% and 0 otherwise.

Any projection of points on a spherical surface onto a two-dimensional plane will result in some undesired effects, such as distortion of bearings and/or distances (Gudmundsson and Alerstam 1998). While distances and therefore areas are not perfectly conserved using rhumb lines, their consistent and easily interpreted representation of direction makes their use appropriate for our study, as we focus on the patterns of atmosphere and sea ice response in different directions from ACs. Alternative methods of regridding were found to be either less intuitive or less consistent than the use of rhumb lines. Great circles provide the shortest distance between two points, yet as their bearing is not constant along their track, their representation in polar coordinates is ambiguous. Decomposing the distance between two points into east–west and north–south components to form a cartesian projection is also ambiguous, as calculating east–west distance before north–south distance gives a different answer to calculating north–south distance first, particularly when near the pole. We show in Fig. S3 that differences resulting from the use of each of these projections compared to the use of rhumb lines are relatively minor. As such, the conclusions derived from our analysis are robust to projection choice. Other studies have employed similar cyclone-centered methods to composite onto distance–azimuth grids for midlatitude cyclones, however, in the absence of any indication otherwise we presume that the azimuth and distance are taken not along rhumb lines but along great circles (Rudeva and Gulev 2011; Ponce de León and Bettencourt 2021).

To establish statistical significance, we use a form of Monte Carlo testing. The regridding and compositing process is performed 20 times with AC dates offset from their true date by 1–20 years, with dates at the end of the record cycled back to become the start of the new offset record. Random samples of SIC anomalies are thereby collected with the same spatial and temporal characteristics as used in the true composite. We then take the maximum and minimum values in the offset composites at each bearing and distance to define the range of natural variability. Values outside of this range in the true composite can therefore be confidently attributed to association with ACs. As the composites offset by one year do not show the same pattern as the true composites, we are able to conclude that the effects of ACs on SIC are not simply the
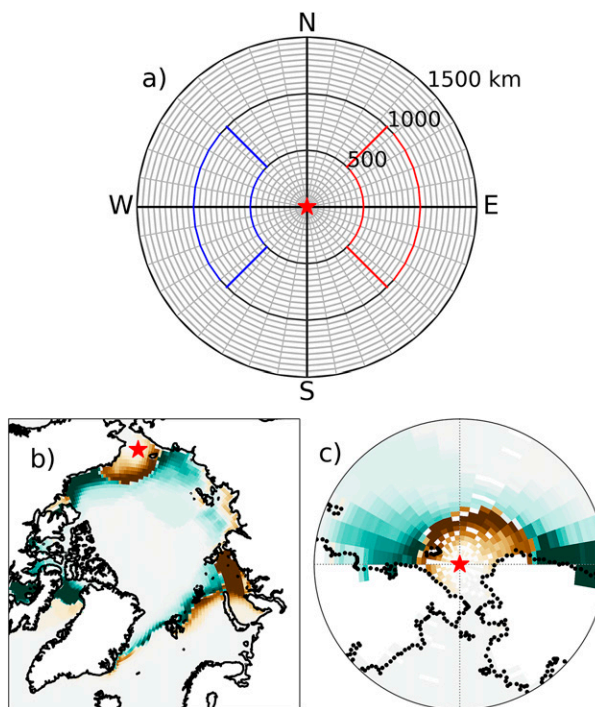

FIG. 3. (a) Grid onto which variables are regridded. The red star indicates Arctic cyclone center location. Blue and red boxes outline the ''west'' and ''east'' sections of the composite used in later analyses. (b) Example of a field of sea ice concentration anomalies plotted in polar stereographic projection. The red star represents a hypothetical Arctic cyclone center location. (c) The example field from (b) regridded onto the grid in (a). Coastline points are also projected onto this grid as a visual aid in this example only.

result of changes in the sea ice mean state or trends in AC properties over time.

3. Results

a. Atmospheric structure of Arctic cyclones

We begin by analyzing the atmospheric structure associated with Arctic cyclones, as this determines their forcing upon Arctic sea ice through surface winds and energy fluxes, and test the degree to which the axisymmetric structure of ACs suggested by Aizawa and Tanaka (2016) applies to our large sample size of ACs in each season.

The characteristic low pressure center associated with ACs is displayed clearly in our composites. A negative SLP anomaly is present in each season, but is strongest in winter and weakest in summer (Fig. 4a). This SLP anomaly is deepest at the cyclone center and is mostly radially symmetrical. The low pressure anomaly drives cyclonic anomalous surface winds (Fig. 4a), which increase in speed from a negligible value at a radius of 1500 km from the AC center to approximately $8\,\mathrm{m\,s^{-1}}$ at a radius of around 300 km. Wind speeds then decrease to much lower values nearer to the cyclone center. As for SLP anomalies, wind speed anomalies are greatest in winter and
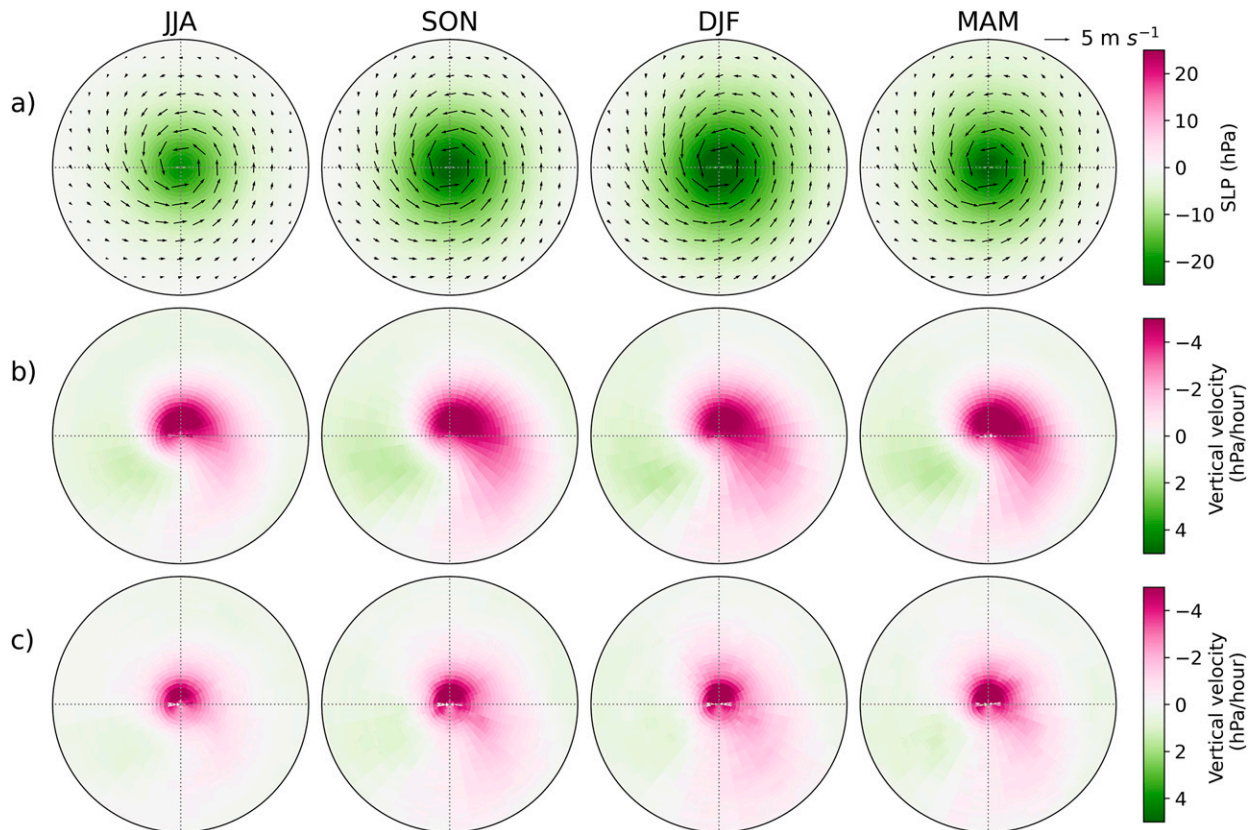
FIG. 4. Atmospheric motion associated with Arctic cyclones in each season. (a) SLP anomaly (shading) and 10-m wind velocity anomaly (arrows, length indicates speed). Vertical velocity at (b) 500 and (c) 900 hPa. Negative values indicate upward vertical motion as pressure coordinates are used.

smallest in summer. Composites of SLP and surface winds without removing the mean annual cycle retain the symmetric pattern, with cyclonic winds (Fig. S4a).

Anomalies in vertical motion at 500 and 900 hPa are also associated with ACs (Figs. 4b,c) as air rises above the low pressure anomaly, and also in a tail extending to the southeast of the AC, while anomalous downward motion occurs away from the AC center. The upward vertical motion is displaced farther north of the AC center at 500 hPa than at 900 hPa, which may qualitatively be explained by the northward slope of a warm front with height. However, we provide a more quantitative alternative explanation in the supplemental material, demonstrating that the combination of anomalous temperatures associated with ACs and the north–south temperature gradient in climatology results in a southwesterly thermal wind, which can explain the observed patterns of 500 hPa vertical motion.

The cyclonic wind pattern drives the advection of warm air from the south to the east of ACs and cold air from the north to the west of ACs. The result is an asymmetrical atmospheric temperature response, with a warm sector to the east of ACs and a cold sector to the west (Fig. 5a shows temperature anomalies at 850 hPa, or T850). Composites of atmospheric temperature at a range of vertical levels indicate that the temperature response is largely equivalent barotropic in the troposphere (Fig. S5). Exceptions to

this include warmer anomalies at the surface level and a shift toward more negative temperatures at higher elevations directly above the AC center. Throughout the troposphere temperature anomalies are on the order of $\pm 4°C$ over large swaths in the warm and cold sectors, respectively. The warm sector temperature anomaly is smaller in summer than in other seasons.

Warm and cold air advection to the east and west of ACs, respectively, is accompanied by anomalous advection of atmospheric water (Fig. 5b, total column water includes water vapor, cloud water, and cloud ice). Warmer air is able to carry more water due to its higher saturation vapor pressure, following the Clausius–Clapeyron relationship. Accordingly, patterns of total column water anomalies associated with ACs mirror those of T850 (Fig. 5a). The total column water patterns are largest in summer, due to the exponential nature of the Clausius–Clapeyron relationship; however, the summer pattern matches the summer T850 pattern less well than in other seasons, which is possibly due to anomalous local heating or moisture sources associated with ACs in summer or again due to nonlinearities in the Clausius–Clapeyron relationship.

Anomalies in atmospheric temperature, water content and vertical motion associated with ACs combine to produce changes in cloud cover (Fig. 5c). Total cloud cover is increased by 7%–13% around the cyclone center depending on season,
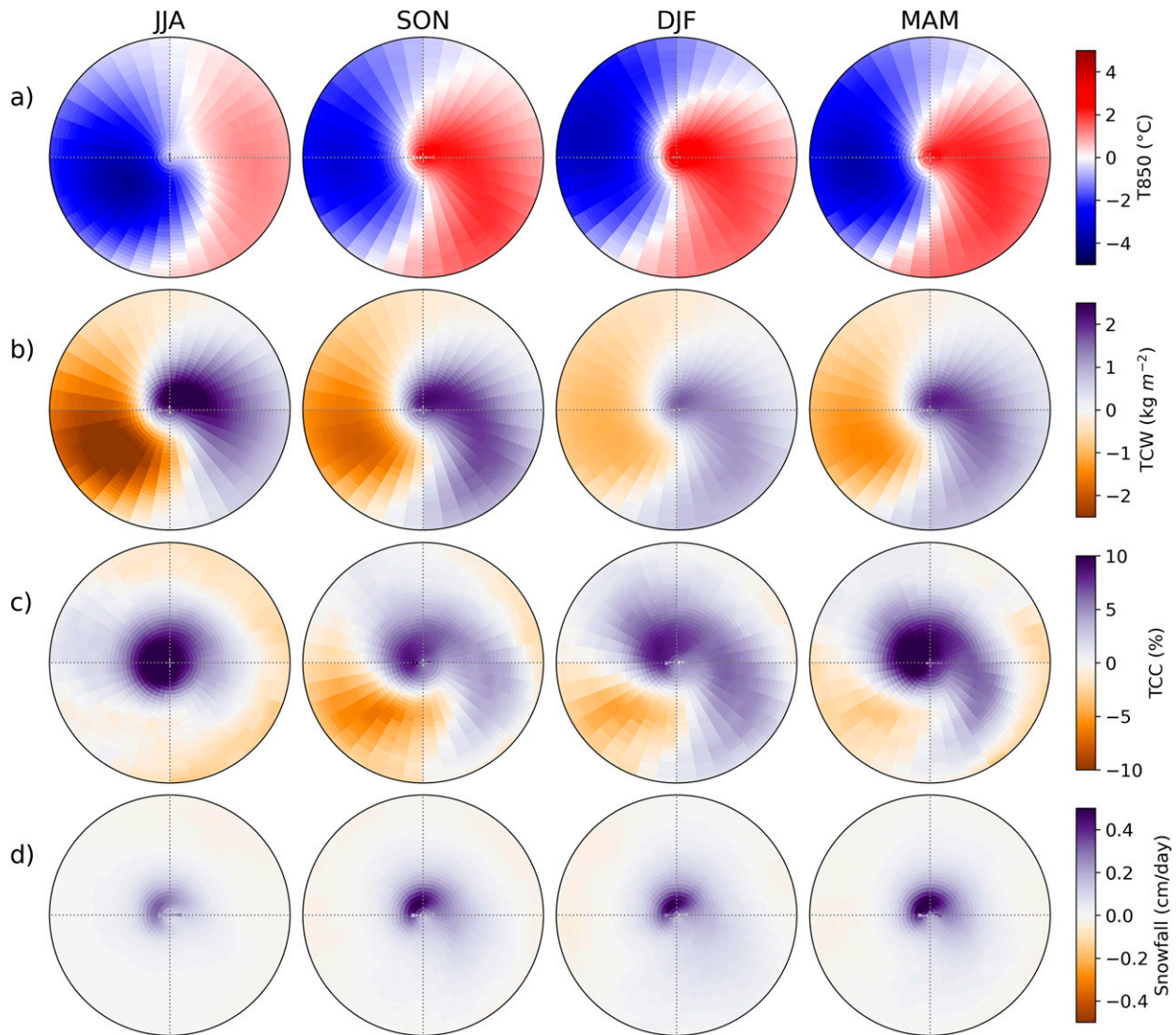
FIG. 5. Atmospheric features associated with Arctic cyclones in each season. (a) T850 anomaly. (b) Total column water anomaly including water vapor, cloud water, and cloud ice. (c) Total cloud cover anomaly. (d) Snowfall anomaly in cm of water equivalent per day.

but also decreased by up to 5% within regions of subsidence (Fig. 4b). A spiraliform cloud pattern is apparent in summer, while a comma cloud form that extends from the AC center along the tail of frontal uplift is apparent in all other seasons. Anomalies in high, medium, and low cloud cover are greater than those in total cloud cover (Fig. S6) due to the cloud overlap effect (Fig. S4b). The largest effects occur at the medium cloud cover level. Our findings are validated by similar composites of cloud cover in ACs found using *CloudSat*, *CALIPSO*, and *ICESat-2* satellite data (Liu and Schweiger 2020).

Snowfall rates are increased around ACs (Fig. 5d), consistent with patterns of uplift (Fig. 4b), cloudiness (Fig. 5c) and atmospheric water content (Fig. 5b). While the impacts of ACs on snowfall are smallest in summer, total precipitation is

increased more in summer than in other seasons (Fig. S7). If a density of 300 kg m^{-3} is assumed for snow on sea ice (Warren et al. 1999; King et al. 2020), then snowfall rates are increased by approximately 1 cm of snow per day in a small region near the AC center in all seasons except summer. Given the large number of ACs in each season (Fig. 1a), the integrated influence on snow cover may be sizable, consistent with Webster et al. (2019), who found that the majority of Arctic snowfall is associated with ACs.

b. Surface energy fluxes associated with Arctic cyclones

Changes in atmospheric temperature, water content and cloudiness alongside changes to the surface ice cover and albedo associated with Arctic cyclones lead to anomalies in the surface energy fluxes (Fig. 6). We composite these fluxes only
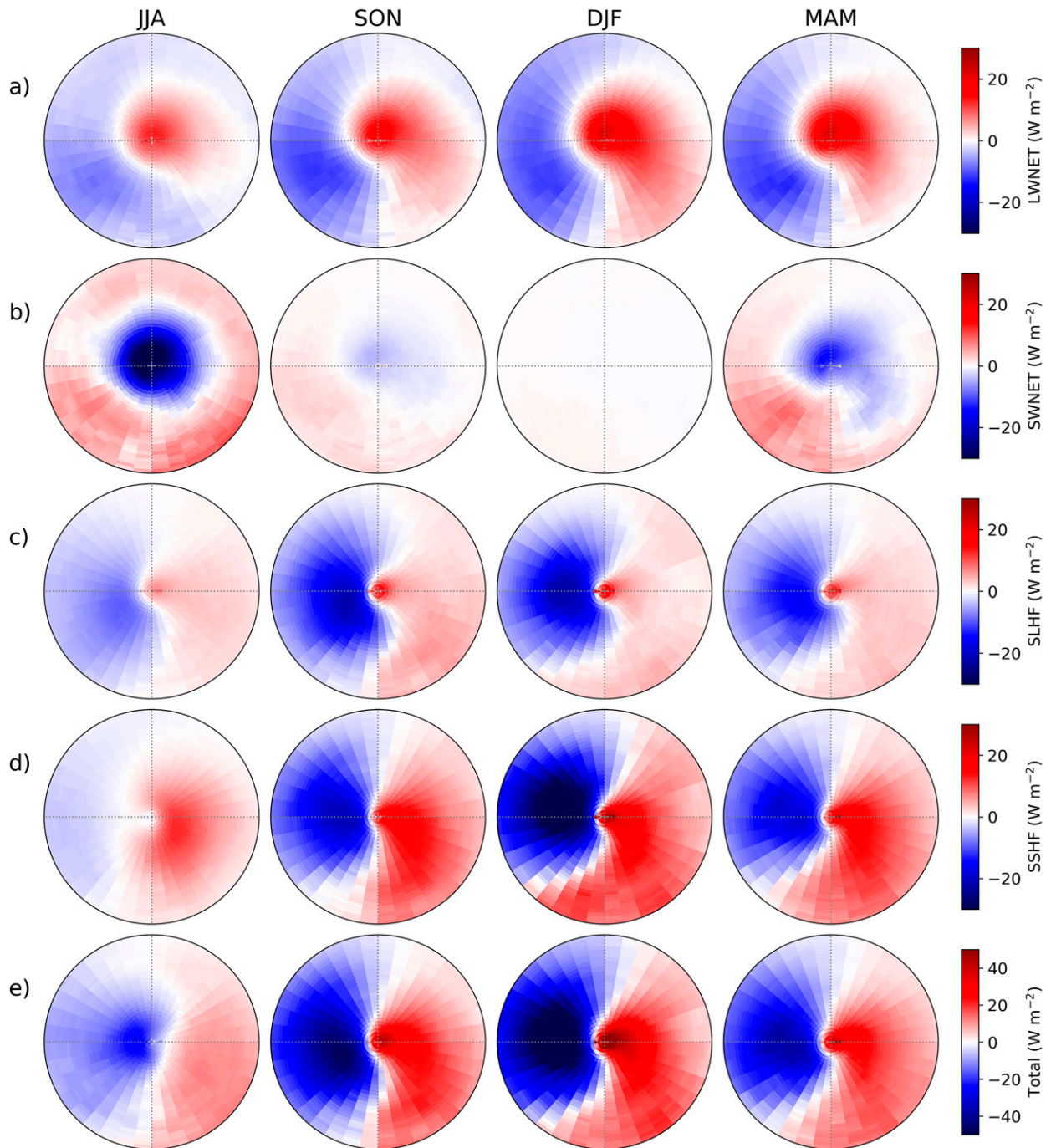
FIG. 6. Surface energy flux anomalies associated with Arctic cyclones in each season. All fluxes are positive downward. (a) Net long-wave. (b) Net shortwave. (c) Surface latent heat flux. (d) Surface sensible heat flux. (e) Total net surface energy flux, equal to the sum of (a), (b), (c), and (d). All composites are taken only over *sea ice regions*.

over what we define as *sea ice regions* (see methods section), as our eventual goal is to understand the influence of ACs on sea ice.

Net longwave flux anomalies (Fig. 6a) reflect a combination of anomalies in atmospheric water content (Fig. 5b), cloud cover (Fig. 5c), and T850 (Fig. 5a), as a warm, cloudy atmosphere emits

more longwave radiation. Accordingly, longwave fluxes are positive (downward) at the AC center and in a tail extending toward the southeast of ACs outside of summer, but negative to the west of ACs. The association of increased downwelling longwave radiation with ACs and/or moisture advection into the Arctic is in agreement with a number of other studies and is
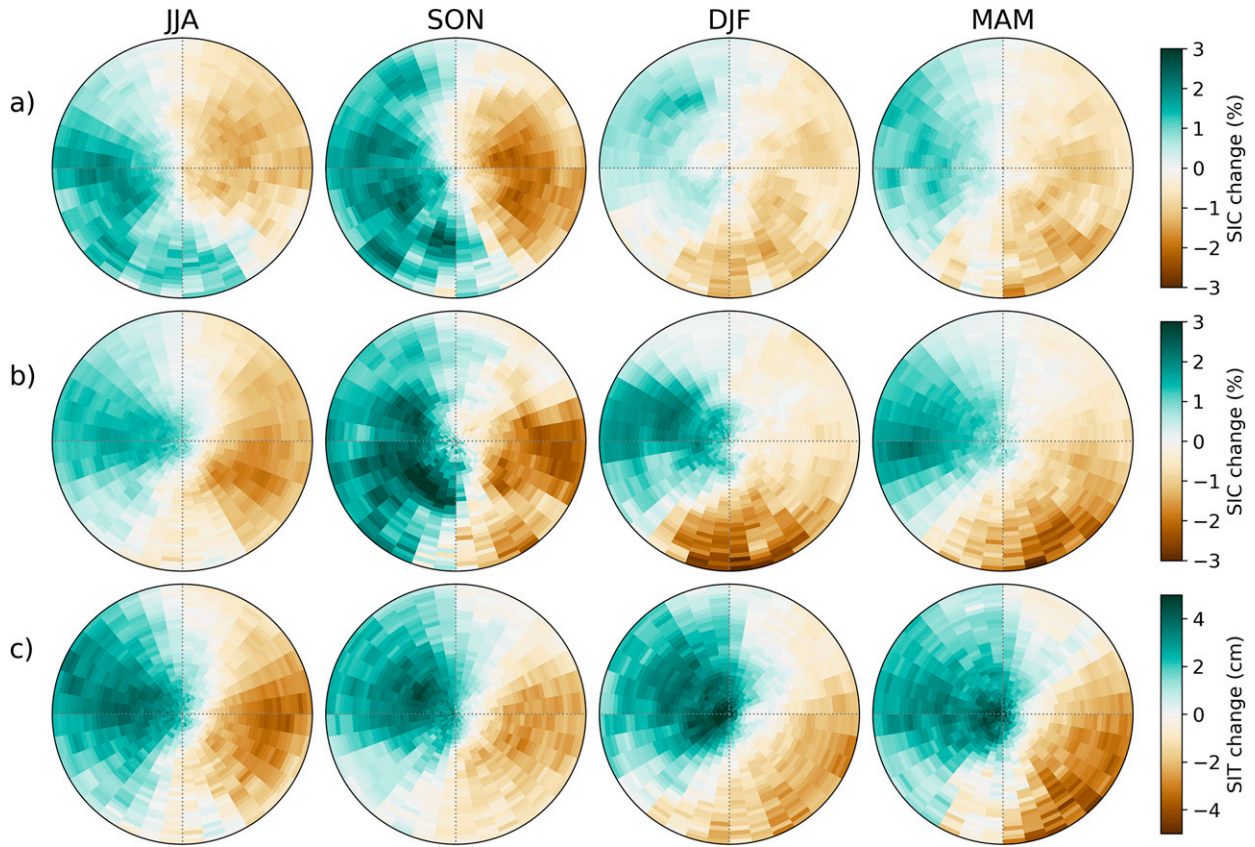
FIG. 7. Sea ice changes associated with Arctic cyclones in each season. (a) SIC change anomalies in observations using Sprenger et al. (2017) AC tracks. See Fig. S9 for equivalent plots using Serreze (2009) AC tracks. (b) SIC change anomalies in CICE5 using Sprenger et al. (2017) AC tracks. (c) SIT change anomalies in CICE5 using Sprenger et al. (2017) AC tracks. In each case the plotted quantity is the anomaly in change in sea ice from 5 days before to 5 days after AC passage over a point.

often tied to surface warming and/or sea ice loss (e.g., Lee et al. 2017; Luo et al. 2017; Finocchio et al. 2020). The net shortwave flux anomalies (Fig. 6b) are of opposite sign to the longwave flux anomalies, owing to the same cloud cover anomalies; however, the magnitude of the shortwave flux anomalies is largest in summer and is virtually zero in winter during polar night. The patterns of downwelling longwave and shortwave flux anomalies at the surface are essentially the same as for net longwave and shortwave flux anomalies, but slightly larger in magnitude (Fig. S8).

Surface latent heat flux (Fig. 6c) and sensible heat flux (Fig. 6d) anomalies are positive (downward) to the east of ACs and negative to the west of ACs in each season. For the most part, this reflects the patterns of anomalies in T850 (Fig. 5a) and atmospheric water content (Fig. 5b). An anomalously warm and moist atmosphere results in reduced heat and moisture transfer from the ocean below in the warm sector, while the opposite effect occurs in the cold sector. The surface sensible heat flux anomaly in summer (Fig. 6d, JJA) is less strongly linked to heat and moisture anomalies than in other seasons, instead showing some similarity with wind speed patterns (Fig. 4a). We hypothesize that this is due to smaller differences between surface and near surface atmospheric

temperatures in summer, allowing boundary layer winds to become the primary control on surface heat transfer.

The net surface energy flux anomaly (Fig. 6e) is equal to the sum of the aforementioned energy flux anomalies (Figs. 6a–d). In each season the net surface energy flux anomaly is positive (downward) in the warm sector to the east of ACs and negative in the cold sector to the west. Anomalies are positive within 100 km of the AC center in fall, winter, and spring, but negative in summer. This is primarily due to the large negative net surface shortwave flux anomaly near the AC center in summer (Fig. 6b, JJA), which is much smaller in other seasons. This difference in surface heating of the atmosphere near the AC center provides a second mechanism in addition to temperature advection that drives negative lower atmospheric temperature anomalies near the AC center in summer but positive anomalies in other seasons (Figs. 5a and S5).

c. Response of sea ice to Arctic cyclones

To investigate how the sea ice responds to the substantial surface wind and energy balance anomalies associated with Arctic cyclones we next analyze how sea ice responds to ACs by calculating composites of SIC and SIT change between 5 days before an AC passes over and 5 days after (Fig. 7).

Positive values indicate that SIC or SIT increases faster or decreases slower than normal at that time of year, while negative values indicate the opposite. We only show the SIT response from CICE5 because of the short time period in which gridded observational SIT datasets are available. The same basic SIC response to ACs is present in observations (Fig. 7a) and CICE5 (Fig. 7b), which gives confidence that the mechanisms through which sea ice responds to ACs are realistically represented in CICE5. The observed SIC response is also recreated when using the Serreze (2009) cyclone tracks (Fig. S9), suggesting that the result is robust to differences in AC-tracking method, which is to be expected given that different extratropical cyclone-tracking algorithms generally produce consistent results for strong cyclones (Neu et al. 2013).

In each season, positive (negative) values between 1% and 3% for SIC change or 1–4 cm for SIT are present to the west (east) of ACs, indicating that ACs drive both anomalous increases and decreases in sea ice depending on its position relative to the AC. The majority of these changes occur within a window of 2 days before the passage of an AC to 2 days after (Fig. S10). Through a Monte Carlo test we find that the patterns in our observed SIC composites lie well outside the range of natural variability (Fig. S11). We find that more intense ACs result in greater SIC change anomalies, and that the pattern of ice increase to the west and decrease to the east of ACs is present for all but the least intense ACs (Fig. S12). These patterns influence high frequency sea ice variability in different regions in different seasons due to differences in the locations of ACs (Fig. 2). For example, outside of summer many ACs occur just south of Svalbard, leading to sea ice loss to the east in the Barents Sea and gain to the west in the East Greenland Sea, while during summer there are fewer ACs affecting these regions and a greater number that might influence the central Arctic.

While our primary objective is to investigate the pattern of the sea ice response to ACs, we also provide estimates of the total sea ice area response to ACs in each season, with further discussion of these results in our supplemental material. The average sea ice area change anomaly associated with an AC is $-978 \, \text{km}^2$ in summer, $-3492 \, \text{km}^2$ in fall, $-9979 \, \text{km}^2$ in winter, and $-1696 \, \text{km}^2$ in spring. These negative values suggest ACs typically result in a small decrease in total Arctic sea ice area, with a great deal of cancellation between the regions of sea ice increase and decrease; however, we note that only calculating the sea ice area change within 1500 km of an AC results in positive sea ice area change anomalies in summer and fall.

To investigate any potential trends in the influence of ACs on Arctic sea ice we perform the same compositing as shown in Fig. 7 but split our AC tracks into those from 1985 to 2000 and 2001–16. In both observations (Figs. S13a,b) and CICE5 (Figs. S13c,d), the east–west differences in SIC change anomalies associated with ACs are present in both periods. This provides further evidence of the robustness of this pattern and suggests that it is relatively consistent over the time period in this study. In both observations and CICE5, the SIC change anomaly is generally greater in magnitude during the second

half of the record than the first in fall, but smaller in spring. Halving our sample size reduces the signal to noise ratio in these composites compared to those using tracks from 1985 to 2016. As a result, it is difficult to determine if the differences between our first and second half composites represent a meaningful change in the influence of ACs on SIC over time.

The composites shown in Fig. 7 present an Arctic-wide average of the effects of ACs on SIC but give no indication as to whether this pattern is ubiquitous across the Arctic. To answer this question, we compute the average SIC change anomaly for each grid cell when it is to the west of an AC and to the east of an AC. Grid cells are defined to be to the west (east) of an AC when they are 500–1000 km from an AC center at a bearing of between 225° and 315° (45°–135°), as indicated by the blue and red boxes in Fig. 3a. The western average minus the eastern average is used as a metric for the strength of the east–west difference in the SIC response to ACs. Discussion of the response of SIC in regions to the north and south of ACs is included in the supplemental material.

We find that the east–west difference in observed SIC response to ACs is up to 20% in all seasons, but mostly only over areas that correspond with the marginal ice zone (Fig. 8). In winter and spring, a substantial response is found almost exclusively in the North Atlantic, while in summer and fall a substantial response is found throughout much of the shelf seas in the central Arctic, where the sea ice concentration has declined dramatically over the period of our analysis. We suggest that the patterns of east–west differences in Fig. 8 are driven by two factors: 1) increased sensitivity of the sea ice cover to ACs at low or medium SIC compared to high SIC and 2) seasonal differences in the spatial distribution of ACs (see Fig. 2). In Fig. 8 we shade regions where fewer than 100 ACs fall within either the western or eastern regions of composites (see boxes in Fig. 3a). Doing so highlights regions where ACs commonly occur, typically coincident with a larger sea ice response, and in which a large sample of ACs improves the signal to noise ratio for each grid cell.

The same procedure to determine the east–west difference in SIC response to ACs was performed using output from CICE5 (Fig. S14). The patterns from CICE5 largely match those from observations (Fig. 8), in both magnitude and spatial distribution in each season. That CICE5 can recreate both the pan-Arctic averaged spatial pattern of SIC response to ACs seen in observations (Figs. 7a,b) and the regional distribution of the east–west component of this pattern gives us confidence that the mechanisms through which ACs influence sea ice are realistically represented in CICE5.

The response of sea ice to ACs can be better understood by compositing SIC and SIT changes partitioned into thermodynamic and dynamic processes using output from CICE5. We integrate the dynamic and thermodynamic tendency anomalies from 5 days before to 5 days after an AC passes over a point (Fig. 9). The changes due to both dynamics and thermodynamics are greatest on the day an AC passes over a point, with the bulk of the changes occurring between 2 days before and 2 days after the AC passes (not shown). The patterns of dynamic SIC and SIT response to ACs are similar to each other and also similar across all seasons, but they have a larger magnitude in winter
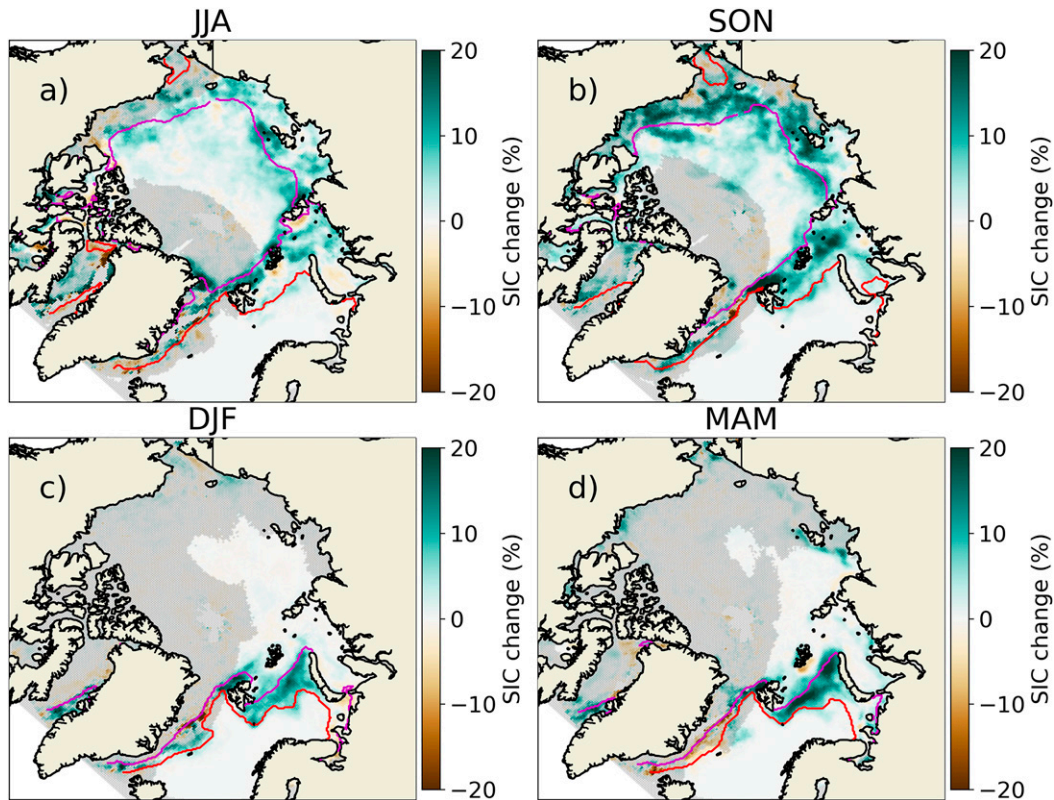
FIG. 8. Observed sea ice concentration change anomalies associated with Arctic cyclones in each season. The plotted quantity is the anomaly in change in SIC from 5 days before to 5 days after a grid cell is to the west of an AC, minus that when it is to the east of an AC (see Fig. 3 for definition of western and eastern regions). The red and magenta lines mark the climatological 15% and 80% SIC contours, respectively. Grid cells where fewer than 100 ACs fall within either the western or eastern regions of composites are shaded in gray.

and spring than summer and fall (Figs. 9a–c). This is perhaps unsurprising, as the surface wind anomaly pattern is similar in each season, but largest in winter (Fig. 4a). Dynamics appear to be the primary driver of the east–west difference in the sign of SIC and SIT responses to ACs, causing ice loss to the east of ACs and ice gain to the west of ACs in each season.

The patterns of thermodynamic SIC response to ACs (Fig. 9b) are roughly equivalent in magnitude to their dynamic equivalents (Fig. 9a) except for in summer when thermodynamics play a lesser role. The thermodynamic SIT response (not shown) is an order of magnitude smaller than its dynamic equivalent (Fig. 9c) in all seasons. This suggests that dynamics and thermodynamics are both important for driving the SIC response to ACs, but dynamics primarily drive the SIT response. The thermodynamic SIC response contributes modestly to the pattern of east–west difference in SIC response to ACs, but only in summer and fall. Perhaps counterintuitively, thermodynamic SIC tendency anomalies are positive in the warm sector of the AC in winter and spring. This may be explained by anticorrelation between dynamic and thermodynamic tendencies, as has been previously noted in GCMs (Blanchard-Wrigglesworth and Bitz 2014). Increased divergence of the sea ice to the east of ACs results in more open water, which quickly

freezes as the atmosphere is still cold, even in the warm sector of the cyclone in these seasons (see Fig. 10d, discussed later).

The sea ice thermodynamic tendency response to ACs in CICE5 can be decomposed into the changes in ice top melt, basal melt, congelation ice growth (thickening of existing ice) and frazil ice growth (growth of new ice in open water), as shown in Fig. 10. Lateral ice melt responses are negligible and therefore not shown.

The influence of ACs on ice top melt rate (Fig. 10a) is large in summer, showing a clear connection to the pattern of net surface energy flux anomalies (Fig. 6e, JJA) and contributing to the east–west pattern of sea ice response to ACs. Outside of summer, ice top melt rate anomalies are close to zero. These seasonal differences can be explained by the necessity for ice to be at its melting point for the surface energy balance to cause melting at the top. For the most part this condition is only met in summer, outside which the ice surface is generally well below freezing.

The influence of ACs on ice basal melt rate (Fig. 10b) is also largest in summer, with a ring of increased melt rates surrounding the AC center. This pattern is very similar to the pattern of wind speeds shown in Fig. 4a. In CICE5, turbulent mixing below the sea ice is parameterized to be closely related
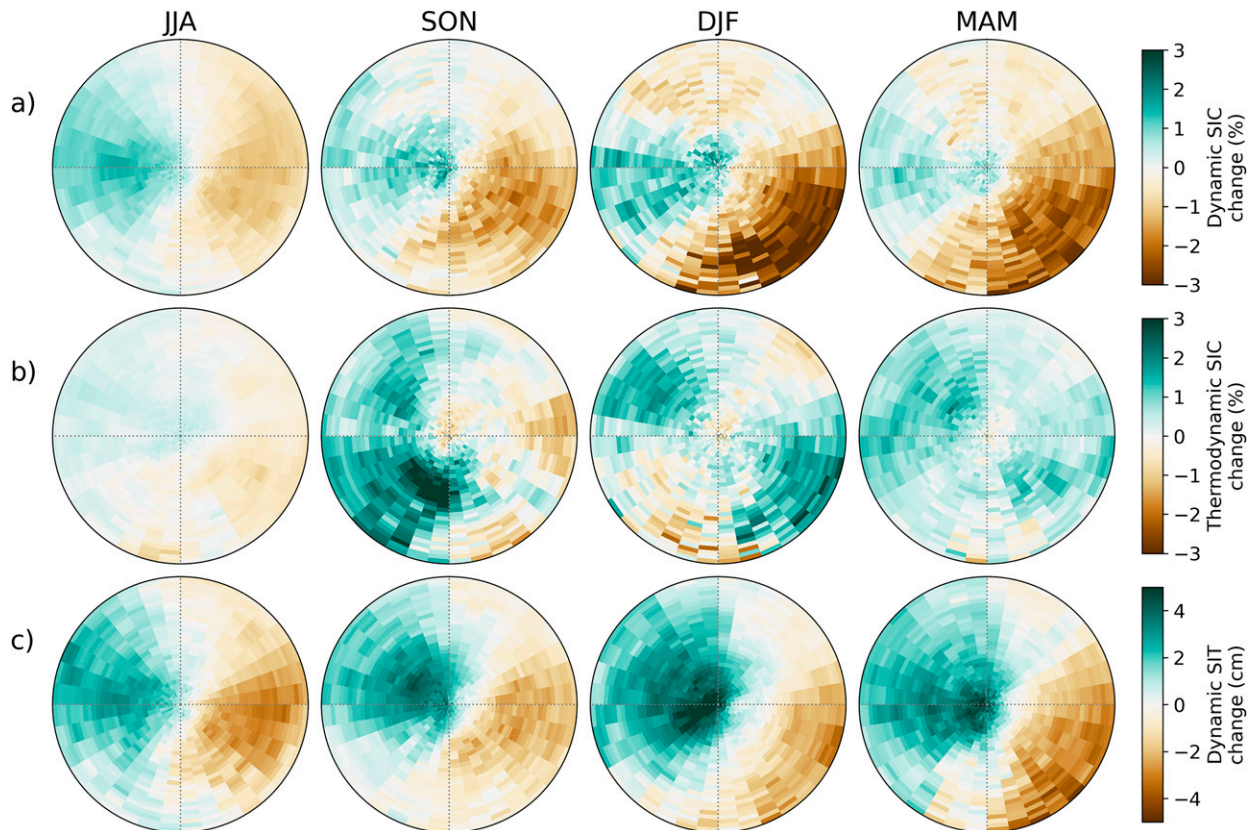
FIG. 9. Thermodynamic and dynamic components of the sea ice response to Arctic cyclones in CICE5. (a) Dynamic SIC change anomaly. (b) Thermodynamic SIC change anomaly. (c) Dynamic SIT change anomaly. Thermodynamic SIT change anomalies are not shown as they are an order of magnitude smaller than dynamic SIT change anomalies. Each plotted quantity is the integrated tendency from 5 days before to 5 days after an AC passes over a point.

to ice motion, which itself is driven by surface winds, explaining the connection. Outside summer, the water near the ice base is essentially always at the freezing point and sea ice is less mobile due to higher concentrations, resulting in reduced influence on ice basal melt despite similar anomalous wind speeds. The use of a slab ocean in our CICE5 run means that the representation of the influence of ACs on ice basal melt may lack some important processes, such as mixed layer ocean dynamics.

The influence of ACs on congelation and frazil ice growth rates (Figs. 10c,d) is near zero in summer, when little ice growth occurs, but substantial in other seasons when compared to melt rates. The pattern of congelation ice growth rate anomalies in some ways reflects the patterns of net surface energy flux anomalies (Fig. 6e) and 2-m surface temperature anomalies (Fig. S5e), although neither provides a full explanation. Additionally, the pattern of existing sea ice and ocean temperatures are key determining factors. Frazil ice growth rate anomalies are largely positive, with a pattern that mirrors that of surface wind speeds (Fig. 4a).

To better understand the dynamic processes that drive the east–west difference in sea ice growth associated with ACs, we composite sea ice drift velocity anomalies from CICE5

(Fig. 11c). We also composite a measure of sea ice volume flux, the sea ice drift velocity multiplied by the ice thickness (Fig. 11e). The cyclonic circulation seen in surface wind anomaly composites from ERA5 (Fig. 11a) is present in both the ice drift and volume flux composites, albeit in a less axisymmetric manner.

We calculate convergence in composites of anomalies in ERA5 surface wind velocity (Fig. 11b), sea ice drift from CICE5 (Fig. 11d) and the ice volume flux from CICE5 (Fig. 11f) as

$$-\nabla \cdot \mathbf{A} = -\frac{1}{r}\left(\frac{\partial r A_r}{\partial r} + \frac{\partial A_\theta}{\partial \theta}\right),$$

where $\mathbf{A}$ is a vector field, of which $-\nabla \cdot \mathbf{A}$ is the convergence, r is the radius and θ is the angle from the AC center and A_r and A_θ are the components of $\mathbf{A}$ in the radial and angular directions, respectively. This calculation provides only an estimate, as it is performed only on the composited averages for each anomaly, which includes some distortion due to the regridding process, which does not perfectly conserve properties such as convergence.

The dynamic thickness tendency anomaly can be calculated as the convergence of the sea ice volume flux. Our estimate
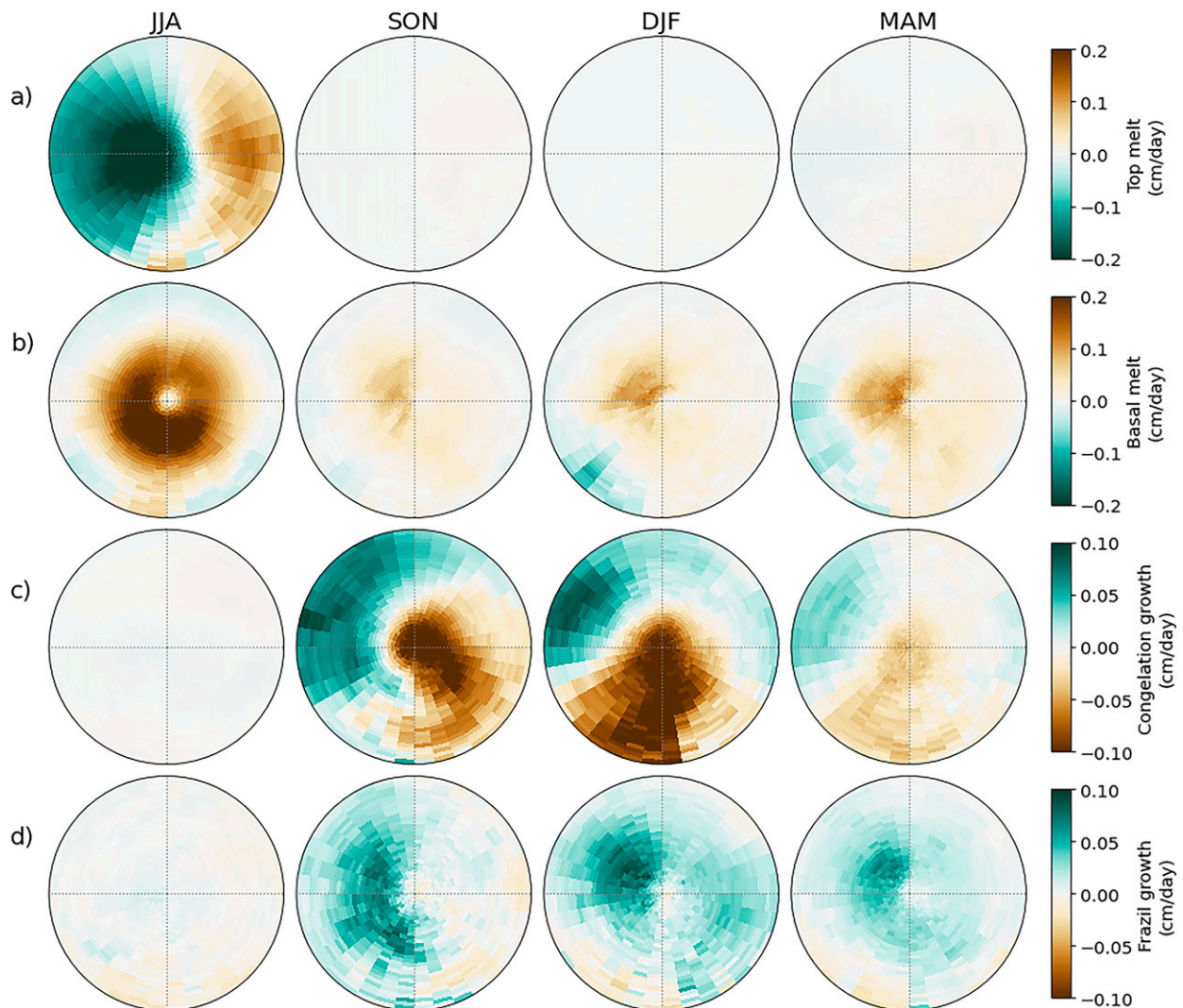
FIG. 10. Sea ice melt and growth response to Arctic cyclones in CICE5. (a) Top melt rate anomaly. (b) Basal melt rate anomaly. (c) Congelation ice growth rate anomaly. (d) Frazil ice growth rate anomaly. Note that ice growth anomalies are plotted on a color scale with half the range of that used for melt anomalies. Each plotted quantity is the rate of change on the day an AC passes over a point.

of this convergence (Fig. 11f) shows good agreement with that calculated by CICE5 (Fig. 9c), with ice convergence (divergence) to the west (east) of ACs, although the magnitude is overestimated. Convergence in the sea ice drift (Fig. 11d) does not show this same asymmetry, except in summer. This suggests that the gradient of sea ice thickness (Fig. S15), on which the sea ice drift field acts, is a key factor in causing sea ice gain to the west of ACs and loss to the east. Generally speaking, thicker ice drifts south into regions of thinner ice or open water, causing a gain in volume to the west of ACs, while thinner ice is advected north, or the ice edge shifts poleward, to the east. The importance of the sea ice mean state in controlling the asymmetric sea ice response to ACs is highlighted by comparison with the axisymmetric pattern of surface wind convergence (Fig. 11a), where winds converge symmetrically at the AC center, consistent with mass balance

requirements implied by the upward vertical motion at the center of ACs (Fig. 4c).

4. Discussion

The structure of the atmosphere associated with Arctic cyclones has previously been considered to be largely axisymmetric (e.g., Aizawa and Tanaka 2016). Yet, in our analysis, we find an axisymmetric structure is limited primarily to the SLP and surface wind anomalies (Fig. 4a). In contrast, we find that most atmospheric features associated with ACs, including vertical motion, temperature anomalies, moisture content, cloud cover, and surface energy flux anomalies, are asymmetric in every season, with clear warm and cold sectors present (Figs. 5 and 6). Spatial compositing on midlatitude cyclones has revealed similar asymmetries in atmospheric water vapor
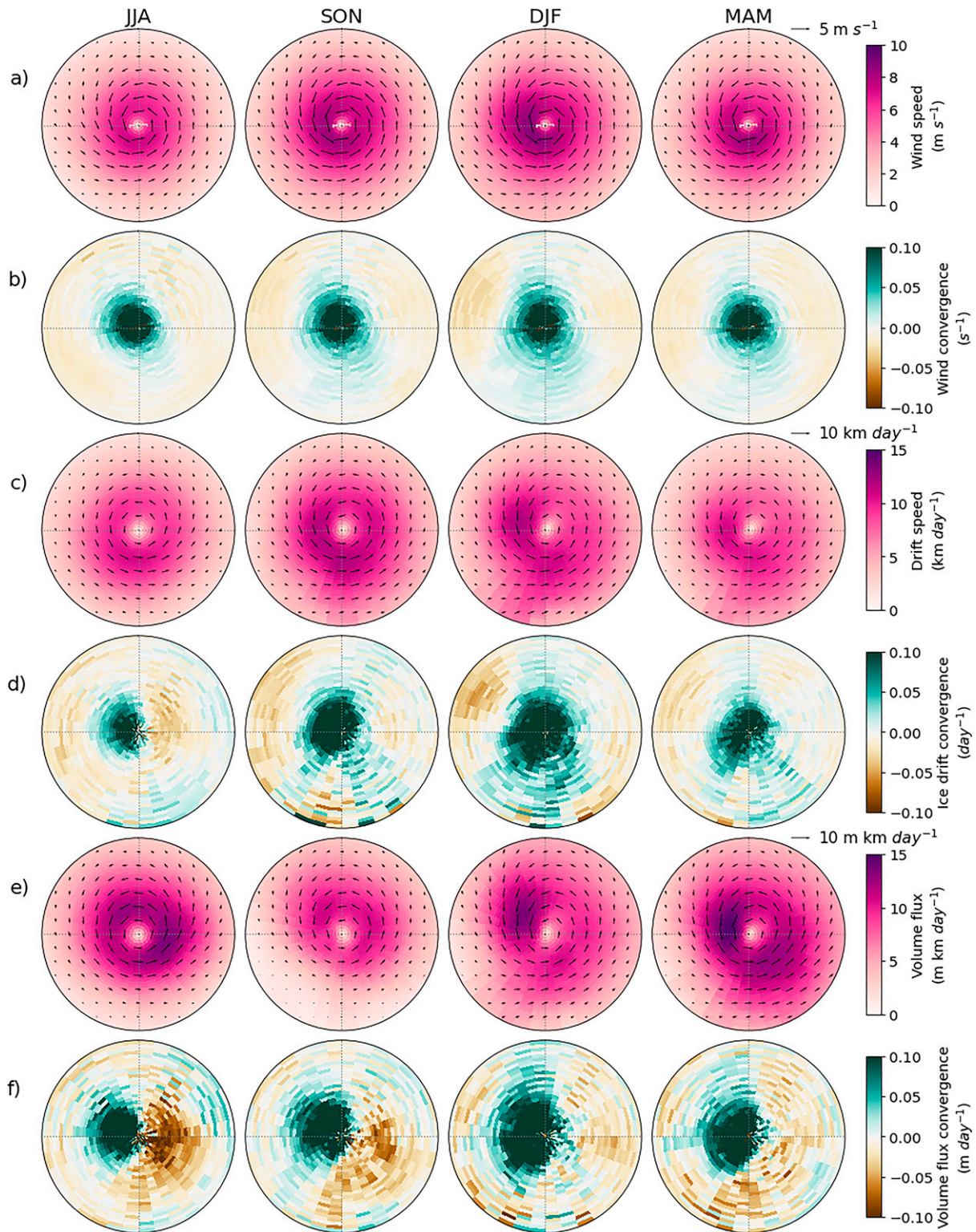
FIG. 11. Convergence and divergence associated with Arctic cyclones. (a) Wind speed (shading) and velocity (arrows) anomalies from ERA5 associated with ACs. (c) Ice drift speed (shading) and velocity (arrows) anomalies from CICE5 associated with ACs. (e) As in (a), but for SIT flux (ice velocity in km day^{-1} multiplied by ice thickness in m). (b),(d),(f) Convergence of the quantities in (a), (c), and (e), respectively.

(Field and Wood 2007), 850 hPa temperature (Catto et al. 2010) and surface turbulent heat fluxes (Rudeva and Gulev 2011). Our surface wind speed and precipitation composites are very similar to those found for midlatitude cyclones in the north and south of both the Atlantic and Pacific (Field and Wood 2007). Catto et al. (2010) and Rudeva and Gulev (2011) find a greater north–south asymmetry in surface wind speeds, which point more toward the cyclone center, and upward vertical motion and precipitation in similar patterns to those in our study, but with maxima farther from the cyclone center. We therefore propose an update to the paradigm for the structure of ACs toward a more asymmetric structure, somewhat comparable to that of a midlatitude cyclone. However, we note that by selecting just the upper quartile of intense ACs, we may be preferentially selecting more mature cyclones.

Total surface energy flux anomalies in winter during ACs in our analysis have peak negative values in excess of $-40 \, \mathrm{W \, m^{-2}}$ over an area several hundred kilometers in diameter to the west of a typical AC and peak positive values of a similar magnitude but over a smaller area at the cyclone center and extending to the east. With total surface flux anomalies varying to this degree, one might expect that the sea ice also would exhibit a strong asymmetry in response to ACs. Indeed, it does, but the anomalously cyclonic sea ice motion induced by the AC in combination with north–south gradients in the background sea ice concentration and thickness are even more important factors driving the asymmetric sea ice response.

The spatial heterogeneity in the response of sea ice to ACs may explain the disagreement among previous studies regarding the total Arctic sea ice area response to ACs (e.g., Simmonds and Keay 2009; Screen et al. 2011). We show not only that the sea ice response to a single AC differs with direction and distance (Fig. 7), but that it differs with the location of the AC and the characteristics of the underlying ice (Fig. 8). We estimate that the typical total Arctic sea ice area response to ACs is very small in each season (see supplemental material) due to cancellation between the regions of ice gain and loss to the west and east of ACs, highlighting that it is difficult to robustly constrain the sign of the total sea ice area response to ACs.

The decrease in sea ice that we find to the east of ACs (Fig. 7) is consistent with that found between a low and high pressure dipole by Wang et al. (2020). The largely axisymmetric pattern of sea ice loss at the center of ACs by Kriegsmann and Brümmer (2014) is not replicated in our study, which we attribute to our use of a consistent north-facing reference frame, inclusion of the marginal ice zone and a much larger AC sample size, as their sample size of 3496 AC observations is often split into four intensity quartiles, while we use a total of 35 069 AC observations even after selecting the upper quartile of ACs. We do, however, confirm their finding that more intense ACs have a greater influence on local SIC.

The larger amplitude of the sea ice response to ACs in the marginal ice zone compared to the interior confirms the findings in Semenov et al. (2019), Schreiber and Serreze (2020),

and Finocchio et al. (2020). Future sea ice decline under global warming may result in a decrease in the extent of high SIC regions in the Arctic and an increase of the proportion of the ice covered by the marginal ice zone, particularly in summer (Strong and Rigor 2013). This may result in an increased impact of ACs on sea ice in the future.

5. Summary and conclusions

In this study we present a new methodology for analyzing the typical spatial patterns associated with Arctic cyclones. Our primary conclusions are as follows:

- Arctic cyclones induce cyclonic winds that, in the presence of spatial gradients in the background state, result in asymmetric structures in the anomalies of atmospheric temperature, moisture content, cloud cover, and vertical motion, with a warm (cold), moist (dry) sector to the east (west) of the cyclone center. This cyclone structure can span diameters in excess of 3000 km.
- This atmospheric structure acts as a forcing on sea ice, with surface energy fluxes influencing the sea ice thermodynamics and surface winds altering sea ice drift and upper ocean mixing.
- The response of sea ice to Arctic cyclones is spatially heterogeneous, with anomalous increases in sea ice to the west of Arctic cyclones and decreases to the east of Arctic cyclones in each season. This response is shown to be relatively constant over the period from 1985 to 2016. The east–west difference in the sea ice concentration response to Arctic cyclones reaches a maximum of 10%–20% over much of the marginal ice zone.
- Despite large east–west variations in the surface energy flux anomalies, this east–west difference in the sea ice response to Arctic cyclones is primarily driven by sea ice dynamics, with ice convergence to the west of cyclones and divergence to the east.
- Arctic cyclones influence sea ice melt and growth rates, with an effect on sea ice concentration comparable in magnitude to that of dynamics.

While it is common for studies to associate Arctic cyclones with a net gain or loss of sea ice, we find that their primary influence is to redistribute sea ice. Accordingly, we propose that Arctic cyclones may be considered a key influence on regional sea ice variability on subseasonal time scales.

REFERENCES

Aizawa, T., and H. L. Tanaka, 2016: Axisymmetric structure of the long lasting summer Arctic cyclones. *Polar Sci.*, **10**, 192–198, https://doi.org/10.1016/j.polar.2016.02.002.

Blanchard-Wrigglesworth, E., and C. M. Bitz, 2014: Characteristics of Arctic sea-ice thickness variability in GCMs. *J. Climate*, **27**, 8244–8258, https://doi.org/10.1175/JCLI-D-14-00345.1.

Catto, J. L., L. C. Shaffrey, and K. I. Hodges, 2010: Can climate models capture the structure of extratropical cyclones? *J. Climate*, **23**, 1621–1635, https://doi.org/10.1175/2009JCLI3318.1.

Cavallo, S. M., and G. J. Hakim, 2010: Composite structure of tropopause polar cyclones. *Mon. Wea. Rev.*, **138**, 3840–3857, https://doi.org/10.1175/2010MWR3371.1.

Comiso, J. C., 2017: Bootstrap sea ice concentrations from Nimbus-7 SMMR and DMSP SSM/I-SSMIS, Version 3. National Snow and Ice Data Center Distributed Active Archive Center, accessed 21 February 2020, https://doi.org/10.5067/7Q8HCCWS4I0R.

Fearon, M. G., J. D. Doyle, D. R. Ryglicki, P. M. Finocchio, and M. Sprenger, 2020: The role of cyclones in moisture transport into the Arctic. *Geophys. Res. Lett.*, **48**, e2020GL090353, https://doi.org/10.1029/2020GL090353.

Field, P. R., and R. Wood, 2007: Precipitation and cloud structure in midlatitude cyclones. *J. Climate*, **20**, 233–254, https://doi.org/10.1175/JCLI3998.1.

Finocchio, P. M., J. D. Doyle, D. P. Stern, and M. G. Fearon, 2020: Short-term impacts of Arctic summer cyclones on sea ice extent in the marginal ice zone. *Geophys. Res. Lett.*, **47**, e2020GL088338, https://doi.org/10.1029/2020GL088338.

Graham, R. M., and Coauthors, 2019: Evaluation of six atmospheric reanalyses over Arctic sea ice from winter to early summer. *J. Climate*, **32**, 4121–4143, https://doi.org/10.1175/JCLI-D-18-0643.1.

Gudmundsson, G. A., and T. Alerstam, 1998: Optimal map projections for analysing long-distance migration routes. *J. Avian Biol.*, **29**, 597–605, https://doi.org/10.2307/3677180.

Hersbach, H., and Coauthors, 2020: The ERA5 global reanalysis. *Quart. J. Roy. Meteor. Soc.*, **146**, 1999–2049, https://doi.org/10.1002/qj.3803.

Hoskins, B. J., M. E. McIntyre, and A. W. Robertson, 1985: On the use and significance of isentropic potential vorticity maps. *Quart. J. Roy. Meteor. Soc.*, **111**, 877–946, https://doi.org/10.1002/qj.49711147002.

Hunke, E. C., W. H. Lipscomb, A. K. Turner, N. Jeffery, and S. Elliott, 2015: CICE: The Los Alamos Sea Ice Model documentation and software user's manual, version 5.1. Doc. LA-CC-06-012, 116 pp., http://www.ccpo.odu.edu/~klinck/Reprints/PDF/cicedoc2015.pdf.

Japan Meteorological Agency, 2013: JRA-55: Japanese 55-year reanalysis, daily 3-hourly and 6-hourly data. NCAR Computational and Information Systems Laboratory Research Data Archive, accessed 1 January 2019, https://doi.org/10.5065/D6HH6H41.

King, J., S. Howell, M. Brady, P. Toose, C. Derksen, C. Haas, and J. Beckers, 2020: Local-scale variability of snow density on Arctic sea ice. *Cryosphere*, **14**, 4323–4339, https://doi.org/10.5194/tc-14-4323-2020.

Kobayashi, S., and Coauthors, 2015: The JRA-55 reanalysis: General specifications and basic characteristics. *J. Meteor. Soc. Japan*, **93**, 5–48, https://doi.org/10.2151/jmsj.2015-001.

Koyama, T., J. Stroeve, J. Cassano, and A. Crawford, 2017: Sea ice loss and Arctic cyclone activity from 1979 to 2014. *J. Climate*, **30**, 4735–4754, https://doi.org/10.1175/JCLI-D-16-0542.1.

Kriegsmann, A., and B. Brümmer, 2014: Cyclone impact on sea ice in the central Arctic Ocean: A statistical study. *Cryosphere*, **8**, 303–317, https://doi.org/10.5194/tc-8-303-2014.

Lee, M.-H., and J.-H. Kim, 2019: The role of synoptic cyclones for the formation of Arctic summer circulation patterns as clustered by self-organizing maps. *Atmosphere*, **10**, 474, https://doi.org/10.3390/atmos10080474.

Lee, S., T. Gong, S. B. Feldstein, J. A. Screen, and I. Simmonds, 2017: Revisiting the cause of the 1989–2009 Arctic surface warming using the surface energy budget: Downward infrared radiation dominates the surface fluxes. *Geophys. Res. Lett.*, **44**, 10 654–10 661, https://doi.org/10.1002/2017GL075375.

Liu, Z., and A. J. B. Schweiger, 2020: Cloud structure of the Arctic cyclone. *2020 Fall Meeting*, San Francisco, CA, Amer. Geophys. Union, Abstract A151-0004.

Lukovich, J. V., J. C. Stroeve, A. Crawford, L. Hamilton, M. Tsamados, H. Heorton, and F. Massonnet, 2021: Summer extreme cyclone impacts on Arctic sea ice. *J. Climate*, **34**, 4817–4834, https://doi.org/10.1175/JCLI-D-19-0925.1.

Luo, B., D. Luo, L. Wu, L. Zhong, and I. Simmonds, 2017: Atmospheric circulation patterns which promote winter Arctic sea ice decline. *Environ. Res. Lett.*, **12**, 054017, https://doi.org/10.1088/1748-9326/aa69d0.

Mayer, M., S. Tietsche, L. Haimberger, T. Tsubouchi, J. Mayer, and H. Zuo, 2019: An improved estimate of the coupled Arctic energy budget. *J. Climate*, **32**, 7915–7934, https://doi.org/10.1175/JCLI-D-19-0233.1.

Neu, U., and Coauthors, 2013: IMILAST: A community effort to intercompare extratropical cyclone detection and tracking algorithms. *Bull. Amer. Meteor. Soc.*, **94**, 529–547, https://doi.org/10.1175/BAMS-D-11-00154.1.

Overland, J. E., and C. H. Pease, 1982: Cyclone climatology of the Bering Sea and its relation to sea ice extent. *Mon. Wea. Rev.*, **110**, 5–13, https://doi.org/10.1175/1520-0493(1982)110<0005:CCOTBS>2.0.CO;2.

Parkinson, C. L., and J. C. Comiso, 2013: On the 2012 record low Arctic sea ice cover: Combined impact of preconditioning and an August storm. *Geophys. Res. Lett.*, **40**, 1356–1361, https://doi.org/10.1002/grl.50349.

Peng, L., X. Zhang, J.-H. Kim, K.-H. Cho, B.-M. Kim, Z. Wang, and H. Tang, 2021: Role of intense Arctic storm in accelerating summer sea ice melt: An in situ observational study. *Geophys. Res. Lett.*, **48**, e2021GL092714, https://doi.org/10.1029/2021GL092714.

Ponce de León, S., and J. H. Bettencourt, 2021: Composite analysis of North Atlantic extra-tropical cyclone waves from satellite altimetry observations. *Adv. Space Res.*, **68**, 762–772, https://doi.org/10.1016/j.asr.2019.07.021.

Rae, J. G. L., A. D. Todd, E. W. Blockley, and J. K. Ridley, 2017: How much should we believe correlations between Arctic cyclones and sea ice extent? *Cryosphere*, **11**, 3023–3034, https://doi.org/10.5194/tc-11-3023-2017.

Rudeva, I., and S. K. Gulev, 2011: Composite analysis of North Atlantic extratropical cyclones in NCEP–NCAR reanalysis data. *Mon. Wea. Rev.*, **139**, 1419–1446, https://doi.org/10.1175/2010MWR3294.1.

Schreiber, E. A. P., and M. C. Serreze, 2020: Impacts of synoptic-scale cyclones on Arctic sea-ice concentration: A systematic analysis. *Ann. Glaciol.*, **61**, 139–153, https://doi.org/10.1017/aog.2020.23.

Screen, J. A., I. Simmonds, and K. Keay, 2011: Dramatic interannual changes of perennial Arctic sea ice linked to abnormal

summer storm activity. *J. Geophys. Res.*, **116**, D15105, https://doi.org/10.1029/2011JD015847.

——, T. J. Bracegirdle, and I. Simmonds, 2018: Polar climate change as manifest in atmospheric circulation. *Curr. Climate Change Rep.*, **4**, 383–395, https://doi.org/10.1007/s40641-018-0111-4.

Semenov, A., X. Zhang, A. Rinke, W. Dorn, and K. Dethloff, 2019: Arctic intense summer storms and their impacts on sea ice—A regional climate modeling study. *Atmosphere*, **10**, 218, https://doi.org/10.3390/atmos10040218.

Serreze, M., 2009: Northern Hemisphere cyclone locations and characteristics from NCEP/NCAR reanalysis data, version 1. NASA National Snow and Ice Data Center, accessed 11 August 2019, https://doi.org/10.5067/XEPCLZKPAJBK.

——, and A. P. Barrett, 2008: The summer cyclone maximum over the central Arctic Ocean. *J. Climate*, **21**, 1048–1065, https://doi.org/10.1175/2007JCLI1810.1.

Simmonds, I., and K. Keay, 2009: Extraordinary September Arctic sea ice reductions and their relationships with storm behavior over 1979–2008. *Geophys. Res. Lett.*, **36**, L19715, https://doi.org/10.1029/2009GL039810.

——, and I. Rudeva, 2012: The great Arctic cyclone of August 2012. *Geophys. Res. Lett.*, **39**, L23709, https://doi.org/10.1029/2012GL054259.

——, and ——, 2014: A comparison of tracking methods for extreme cyclones in the Arctic basin. *Tellus*, **66A**, 25252, https://doi.org/10.3402/tellusa.v66.25252.

Sprenger, M., and Coauthors, 2017: Global climatologies of Eulerian and Lagrangian flow features based on ERA-Interim. *Bull. Amer. Meteor. Soc.*, **98**, 1739–1748, https://doi.org/10.1175/BAMS-D-15-00299.1.

Stern, D. P., J. D. Doyle, N. P. Barton, P. M. Finocchio, W. A. Komaromi, and E. J. Metzger, 2020: The impact of an intense cyclone on short-term sea ice loss in a fully coupled atmosphere-ocean-ice model. *Geophys. Res. Lett.*, **47**, e2019GL085580, https://doi.org/10.1029/2019GL085580.

Strong, C., and I. G. Rigor, 2013: Arctic marginal ice zone trending wider in summer and narrower in winter. *Geophys. Res. Lett.*, **40**, 4864–4868, https://doi.org/10.1002/grl.50928.

Thorndike, A. S., and R. Colony, 1982: Sea ice motion in response to geostrophic winds. *J. Geophys. Res.*, **87**, 5845–5852, https://doi.org/10.1029/JC087iC08p05845.

Vessey, A. F., K. I. Hodges, L. C. Shaffrey, and J. J. Day, 2020: An inter-comparison of Arctic synoptic scale storms between four global reanalysis datasets. *Climate Dyn.*, **54**, 2777–2795, https://doi.org/10.1007/s00382-020-05142-4.

Wang, Z., J. Walsh, S. Szymborski, and M. Peng, 2020: Rapid Arctic sea ice loss on the synoptic time scale and related atmospheric circulation anomalies. *J. Climate*, **33**, 1597–1617, https://doi.org/10.1175/JCLI-D-19-0528.1.

Warren, S. G., I. G. Rigor, N. Untersteiner, V. F. Radionov, N. N. Bryazgin, Y. I. Aleksandrov, and R. Colony, 1999: Snow depth on Arctic sea ice. *J. Climate*, **12**, 1814–1829, https://doi.org/10.1175/1520-0442(1999)012<1814:SDOASI>2.0.CO;2.

Webster, M. A., C. Parker, L. Boisvert, and R. Kwok, 2019: The role of cyclone activity in snow accumulation on Arctic sea ice. *Nat. Commun.*, **10**, 5285, https://doi.org/10.1038/s41467-019-13299-8.

Yamagami, A., M. Matsueda, and H. L. Tanaka, 2017: Extreme Arctic cyclone in August 2016. *Atmos. Sci. Lett.*, **18**, 307–314, https://doi.org/10.1002/asl.757.

Zhang, J., R. Lindsay, A. Schweiger, and M. Steele, 2013: The impact of an intense summer cyclone on 2012 Arctic sea ice retreat. *Geophys. Res. Lett.*, **40**, 720–726, https://doi.org/10.1002/grl.50190.